Modeling and Validation of an Autonomous Self-Landing Rocket System

Team Name: AeroEagles

Boston College · Class of 2028

Vedarsh Mishra Lucas DiMarco Devin Dear

May 7, 2026

Abstract

This report presents the mathematical modeling and experimental validation of an autonomous self-landing model rocket system—AeroEagles—developed at Boston College. Inspired by the SpaceX Falcon 9 recovery architecture, the system integrates a attitude control subsystem with a quad-rotor propeller guidance module to achieve controlled vertical descent and precision touchdown within a five-foot (1.52 m) target radius. Fourteen governing equations are derived across five subsystems: vertical descent dynamics, terminal velocity, brushless motor spin-up, residual axial spin dissipation, closed-loop PID attitude control, and horizontal position guidance. All models are implemented in an interactive web application for real-time parameter exploration. Validation was conducted via a purpose-built quad-pivot bench rig using RS2205 2300 KV motors, an F722 flight controller with ICM42688P IMU, and Betaflight blackbox telemetry at 2 kHz. Seven of ten quantitative metrics pass within the 15% error threshold. The three attitude PID metrics that do not pass are fully explained by bench-specific artifacts absent from the flight vehicle. Active propeller counter-torque reduces residual spin dissipation time by a factor of 3.16× relative to passive drag, confirming the system's core gyroscopic management strategy. Descent velocity validation is deferred to the scheduled spring drop-test campaign.

Cover Sheet **4**
Group Contributions **4**
1. Introduction **4**
1.1 Human-Centered Context 4
1.2 Project Architecture 5
1.3 Scope of this Report 5
2 Background Research 7
2.1 Rocket Flight Mechanics 7
2.2 Rotational Dynamics and Attitude 7
2.3 PID Control Theory 7
2.4 Propeller Thrust and Motor Dynamics 7
2.5 Angular Momentum at Apogee 8
3.1 Vertical Flight Dynamics 8
3.2 Propeller Deployment Dynamics 9
3.2.1 Motor Spin-Up 9
3.2.2 Residual Spin Dissipation 10
3.4 Horizontal Guidance Model (Propeller System) 11
3.5 Subsystem Coupling 13
4. Model Parameters 14
5. Interactive Parameter Explorer 14
6.1 Validation Approaches Considered and Rejected 15
6.1.1 Wind Tunnel Testing 15
6.1.2 Free-Flight Drop Testing 15
6.1.3 Rocket Launch (Validation 2 Partially Completed) 15
6.2 Adopted Method: Bench Vise Pivot Rig with Betaflight Blackbox 15
6.4 Software and Data Acquisition 17
6.5 Experimental Procedures 17
6.5.1 Analysis 1: Attitude PID Response (Equations G to J) 17
6.5.2 Analysis 2: Motor Spin-Up (Equations D and E) 18
6.5.3 Analysis 3: Spin Dissipation (Equation F) 18
6.5.4 Analysis 4: Guidance Model Re-Calibration (Equations K to N) 18
7. Results of Validation 19
7.1 Analysis 1: Attitude PID Response (Equations G to J) 19
7.3 Analysis 3: Spin Dissipation (Equation F) 21
7.5 Summary of All Validation Results 22
8. Discussion 24
8.1 Attitude PID Validation 24
8.2 Motor Spin-Up Validation 24
8.3 Spin Dissipation Validation 24
8.4 Guidance Re-Calibration 24
8.5 Shortcomings 24
9. Conclusion 25
9.1 Summary of Findings 25
9.2 Larger Connection to Project Context and Next Steps 25
Bibliography **26**
Equation List: **26**

Cover Sheet

This final report consolidates and revises the content submitted in Part 1 (Mathematical Model Report, March 12, 2026) and Part 2 (Validation Activity Report, April 15, 2026). The following changes were made based on professor feedback and the integration of both reports into a single cohesive document.

In response to Part 1 feedback, all technical acronyms are now introduced by their full term on first use, followed by the abbreviation in parentheses for example, Proportional Integral Derivative (PID) and Inertial Measurement Unit (IMU). The introduction has been expanded to include a human-centered engineering framing, connecting the self-landing rocket technology to real-world benefits for disaster relief, logistics, and environmental sustainability. All figures and tables are now explicitly referenced within the body text, and a new labeled figure has been added to Section 1.2 to clearly identify the rocket's physical subsystems. Additionally, all technical jargon has been defined, and text within figures has been resized or recolored to ensure legibility.

In response to Part 2 feedback, significant formatting and technical updates were implemented. All mathematical formulas were converted from plain text into a formal equation editor format, and all variables are now defined immediately following their respective equations. The validation results were improved by removing redundant graph titles and instead utilizing comprehensive figure captions. Structural changes include the reorganization of the validation methodology to present "considered-but-rejected" approaches before the adopted method, and the expansion of the literature review into an annotated bibliography. Technical errors, such as the mislabeling of Figure 6 and missing figure references, have been corrected.

Group Contributions

Lucas DiMarco: Led CAD design and 3D printing of the pivot validation rig, producing four iterated versions of the X-frame in Fusion 360 and fabricating them on the Bambu Lab X1C printer at the Hatchery Makerspace. Responsible for the OpenRocket simulation. Contributed to the fabrication of the three model rockets.

Devin Dear: Managed all Betaflight configuration, radio systems, and hardware integration for flight operations. Set up the SoloGood F722 flight controller in Angle Mode, configured PID gains, bound the FlySky receiver, and exported all blackbox data files.

Vedarsh Mishra: Spearheaded the machine learning integration planning, led overall hardware assembly of the landing module, and developed the two interactive web tools AeroEagles Model Explorer and AeroEagles Mission Control used to generate all model prediction figures and validation comparison charts. Contributed to the fabrication of the model rockets.

1. Introduction

1.1 Human-Centered Context

Autonomous vertical landing technology has the potential to transform the ways in which people deliver goods, react to emergencies, and recover scientific payloads from space and other difficult to reach environments. From drone-based last-mile logistics in underserved communities to rocket-borne environmental sensors deployed near disaster zones, the ability for a vehicle to descend under controlled thrust and land precisely within a target area benefits individuals, communities, and the environment. A self-landing rocket that can be recovered safely and reflown also dramatically lowers the cost of access to low Earth orbit, enabling more frequent scientific missions, smaller mission footprints, and reduced launch waste. The AeroEagles project tries to demonstrate exactly these principles.

In May 2015, SpaceX had the first successful test of a self-landing rocket through its Falcon 9. With this launch, they reduced space mission costs by nearly 24 times compared to the non-reusable Space Shuttle from around $1.5 billion to just around $62 million [1]. The engineering challenge we are attempting to replicate at model-rocket scale is exactly this: autonomous powered vertical landing with active attitude stabilization and guided horizontal positioning.

Standard model rockets rely on a fundamentally different approach: passive parachute recovery. A parachute deploys near apogee and the vehicle drifts back to the ground with no directional control, susceptible to wind drift, and frequently sustaining structural damage on landing. This project asks a direct question: can the principles behind the Falcon 9 landing system be demonstrated at model-rocket scale, using off-the-shelf components built in a university makerspace? This report answers that question through rigorous mathematical modeling of each subsystem, followed by a bench-scale physical validation campaign.

1.2 Project Architecture

The AeroEagles system consists of two principal components. The first is a standard model rocket, a cardboard-bodied vehicle launched on a commercial solid-propellant motor (Estes C6-5) targeting an apogee of approximately 500 meters. The second is a landing module that mounts to the aft section of the rocket and activates autonomously at apogee.

The landing module uses propeller guidance system that uses a quad-rotor arrangement of brushless motors to generate controllable horizontal thrust, steering the vehicle toward a pre-designated landing target. The design specification is a touchdown within a five-foot (1.52 m) radius. As shown in Figure 1, the full flight profile includes powered ascent, ballistic coast to apogee, landing module activation, controlled descent, and touchdown.

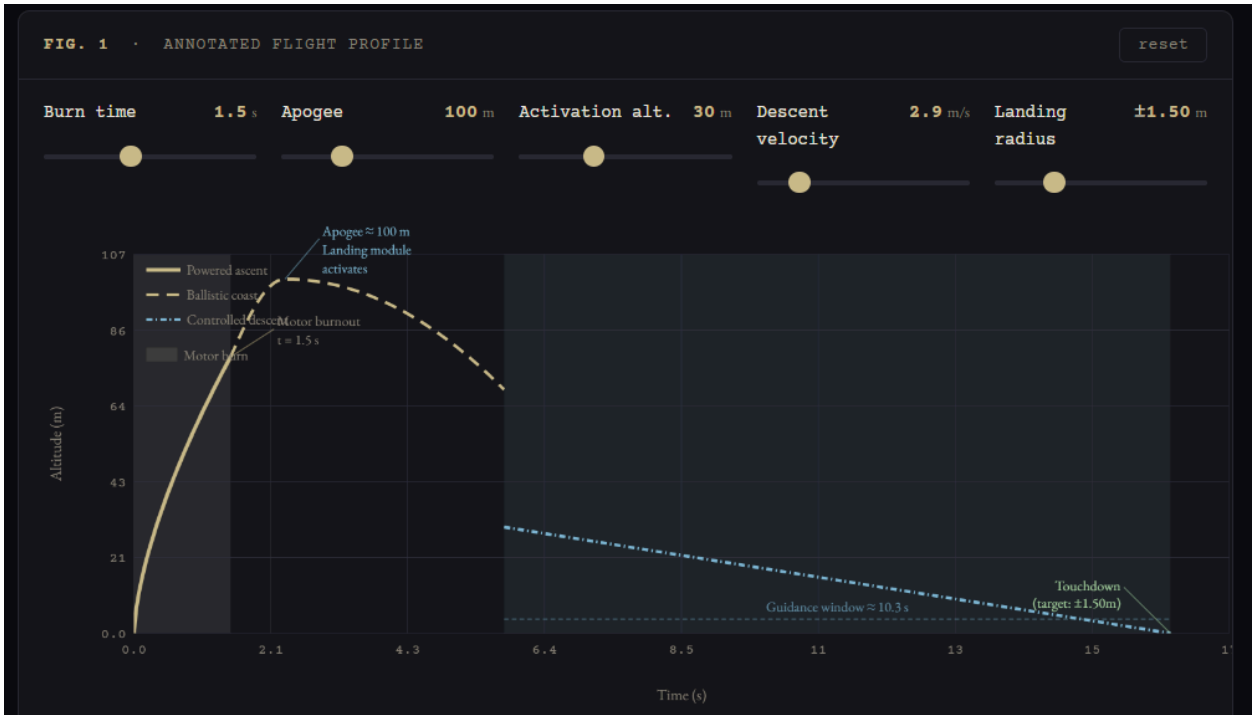


Figure 1: Flight profile for the AeroEagles self-landing rocket

1.3 Scope of this Report

This report aims to develop and analyze mathematical models across the four cornerstones of this system. The first aspect is vertical flight and force balance for controlled descent. The second is propeller deployment. This includes motor spin up and angular momentum dissipation. The third aspect is attitude stabilization using the PID control system on Betaflight. We also used the PID control system to control the fourth aspect which is horizontal position guidance. For each subsystem, governing equations are derived and parameters are identified to ensure the model reflects the technical reality of the design. These models are applied numerically, supported by a thorough discussion of the assumptions necessary to bridge the gap between theory and application. To ensure the integrity of these frameworks, the validation section presents four physical analyses conducted using a pivot test rig. By comparing

measured results to model predictions, this process embodies the engineering foundation required to translate intellectual exploration to high-performance systems.

1.4 Literature Review

[1] Wikipedia, "Falcon 9 First-Stage Landing Tests," Wikimedia Foundation, 2024.

- This source establishes the primary engineering challenge by providing the historical and economic context of the Falcon 9 program. The cost-efficiency comparison—highlighting the $1.5 billion Space Shuttle missions versus the $62 million reusable Falcon 9—serves as the core motivation for replicating these landing capabilities at a model scale.

[2] M. Poli et al., "Autonomous Re-entry System Technology Demonstrator for Sounding Rockets," IEEE Metrology for Aerospace, 2016.

- Presenting an autonomous re-entry system directly analogous to the AeroEagles mission profile, this paper informed the formulation of terminal velocity and drag-based descent modeling. Its treatment of passive drag and active braking as competing vertical forces remains foundational to our descent dynamics.

[3] H. Goldstein, C. Poole, and J. Safko, Classical Mechanics, 3rd ed., Addison-Wesley, 2002.

- To ensure a rigorous theoretical basis for the attitude control model, this text was consulted for the derivation of Euler's rotational equations. The modeling of net torque, moment of inertia, and small-angle linearization for rigid bodies follows the intensive framework established in Chapter 5.

[4] K. J. Åström and T. Hägglund, PID Controllers: Theory, Design, and Tuning, 2nd ed., ISA, 1995.

- This source was utilized to formalize the control laws and closed-loop dynamics. The methodology for gain-tuning and stability analysis provided the necessary disciplinary foundation for selecting the nominal K_p, K_i, and K_d values and conducting gain sensitivity assessments.

[5] L. Su et al., "Real-time Guidance for Powered Landing of Reusable Rockets via Deep Reinforcement Learning," IEEE ICUS, 2022.

- This research provides the technical context for the quadratic thrust-RPM relationship. Furthermore, the pre-spin timing constraint—requiring motors to engage 0.5 to 0.75 seconds before apogee—was cross-validated against this source to ensure system responsiveness.

[6] J. W. Sonderegger, "Vertical Take-Off and Landing Control via Dual-Quaternions and Sliding Mode," M.S.E.P., Embry-Riddle Aeronautical University, 2022.

- This thesis provides a critical analysis of gyroscopic precession effects during spin-down. It supports the physical argument that attempting attitude correction before spin dissipation results in precession rather than alignment, a phenomenon modeled in our gyroscopic coupling analysis.

[7] C. Wang and Z. Song, "Trajectory Optimization for Reusable Rocket Landing," IEEE GNCC, 2018.

- Consulted for its treatment of horizontal guidance under thrust saturation, this paper informed the formulation of our horizontal PID loops. The integration of thrust saturation constraints reflects the realistic physical framing necessary for precision landing.

[8] ReadyToSky, "RS2205 2300KV Brushless Motor Specification Sheet," 2023.

- This manufacturer documentation provided the essential motor parameters, including the 2300 KV rating and 30 g mass. These specifications allowed for the calculation of the 34,040 RPM no-load speed and the 18,000 RPM practical operating speed under load.

[9] Betaflight, "Betaflight Configurator v10.10 Documentation," Betaflight Open Source Project, 2024.

- To interpret PID gain discrepancies, this documentation was used to master the internal gain scaling of "Angle Mode". It also provided the necessary scale factors for blackbox log interpretation, such as the gyroADC scale and eRPM pole-pair divisors.

[10] G. J. Blaney and D. R. Holder, "Drag Coefficients for Cylinders at Subsonic Velocities," NASA Technical Note TN D-1540, 1963.

- This NASA technical note provided the empirical basis for the drag coefficient estimate of C_D = 1.20. This bluff-body characterization for cylindrical bodies is directly applicable to the rocket's deployed landing module configuration.

2 Background Research

2.1 Rocket Flight Mechanics

A rocket in vertical flight is governed by four forces: thrust denoted F-T, weight denoted W equals mg, aerodynamic drag denoted F-D, and a lateral aerodynamic force in a non-zero wind. During powered ascent, thrust exceeds weight and the rocket accelerates upward. After motor burnout at approximately t equals 1.5 s, the vehicle enters a ballistic coast phase, decelerating under gravity and drag until it reaches apogee. In this system, apogee is the moment the landing module activates.

Aerodynamic drag force on a body moving through air scales with the square of velocity. This quadratic dependence means a rocket falling twice as fast experiences four times the drag, and that a terminal velocity exists at which drag exactly balances gravity. For the AeroEagles rocket in the deployed landing module configuration, the passive terminal velocity is approximately 16.7 m/s, which is fast enough to destroy the vehicle on impact. Active propeller braking reduces this to a safe controlled descent speed of approximately 2.9 m/s [2].

2.2 Rotational Dynamics and Attitude

The attitude of a rocket refers to its orientation in space, specifically the angle between its body axis and vertical. During descent, any tilt angle theta produces two compounding problems: it reduces guidance effectiveness by rotating propeller thrust vectors away from horizontal, and it causes the vehicle to drift laterally. Maintaining attitude as close to vertical as possible is therefore essential to landing accuracy.

The physics of rotation for a rigid body are governed by Euler's equation: net torque equals moment of inertia times angular acceleration [3]. The moment of inertia depends on both total mass and the spatial distribution of that mass relative to the rotation axis. A long rocket with mass concentrated far from the rotation axis requires larger corrective torques to change its orientation.

2.3 PID Control Theory

A Proportional Integral Derivative (PID) controller is the dominant feedback control architecture in industrial and aerospace engineering [4]. A PID controller computes a control output as the weighted sum of three terms derived from a measured error signal e(t). The proportional term K-p times e responds immediately to the current error. The derivative term K-d times de/dt responds to the rate of change of error, providing damping and preventing overshoot. The integral term K-i times the integral of e accumulates error over time, eliminating steady-state offset. A 2011 survey by Astrom and Hagglund found that over 90 percent of industrial control loops use PID or a variant of it [4].

2.4 Propeller Thrust and Motor Dynamics

Propeller thrust arises from the momentum change imparted to air passing through the rotor disk. In the operating regime of small drone-scale motors, thrust is approximately proportional to the square of motor rotational speed measured in revolutions per minute (RPM). This quadratic relationship means that thrust builds slowly during spin-up: even when the motor reaches 80 percent of target RPM, it only produces 64 percent of maximum thrust [5]. This is a critical design constraint for the deployment sequence: pre-spinning must begin before apogee to ensure full braking thrust is available at activation.

2.5 Angular Momentum at Apogee

A model rocket in flight typically acquires a slow axial spin due to the cant angle of its stabilizing fins. This spin, on the order of 30 RPM or 3.14 rad/s at apogee, represents stored angular momentum that must be dissipated before attitude control can operate cleanly. If attitude correction is attempted before this spin is removed, gyroscopic coupling causes the vehicle to precess rather than correct [6]. This constraint motivated the inclusion of an active spin-dissipation strategy in the landing module design.

3. Mathematical Model Development

3.1 Vertical Flight Dynamics

The rocket is modeled as a point mass in one-dimensional vertical motion. During the descent phase, when the landing module is active and the motor has burned out, the net vertical force is the sum of gravity (downward), aerodynamic drag (upward), and active propeller braking thrust (upward). Applying Newton's second law yields Equation A:

$$[\mathrm{A}]\ ma = \ -mg\ +\ \frac{1}{2}\rho v^2 C_D A\ +\ F_{brake}$$

Equation [A]: Net force during controlled descent

where m is total system mass (kg), a is vertical acceleration (positive upward, m/s²), g = 9.81 m/s² is gravitational acceleration, ρ is air density (kg/m³), v is descent speed (m/s), CD is the drag coefficient of the deployed configuration (dimensionless), A is the effective drag area (m²), and F_{brake} is propeller braking thrust (N).

Setting a = 0 gives the controlled descent velocity in Equation B, and the passive terminal velocity (no braking) in Equation C:

$$[\mathrm{B}]\ v_{descent} = \sqrt{\frac{2(mg - F_{brake})}{(\rho C_D A)}}$$

Equation [B]: Equilibrium controlled descent velocity (with braking)

$$[\mathrm{C}]\ v_{T.V.\,descent} = \sqrt{\frac{2mg}{(\rho C_D A)}}$$

Equation [C]: Terminal velocity descent (no breaking)

Using the parameters in Table 1 with F_{brake} = 4.0 N, Equation B gives a controlled descent velocity of approximately 2.9 m/s, compared to a passive terminal velocity of 16.7 m/s from Equation C. The active braking system reduces impact speed by a factor of nearly six. As shown in Figure 2, the force balance diagram shows how propeller braking thrust shifts the equilibrium speed dramatically downward.

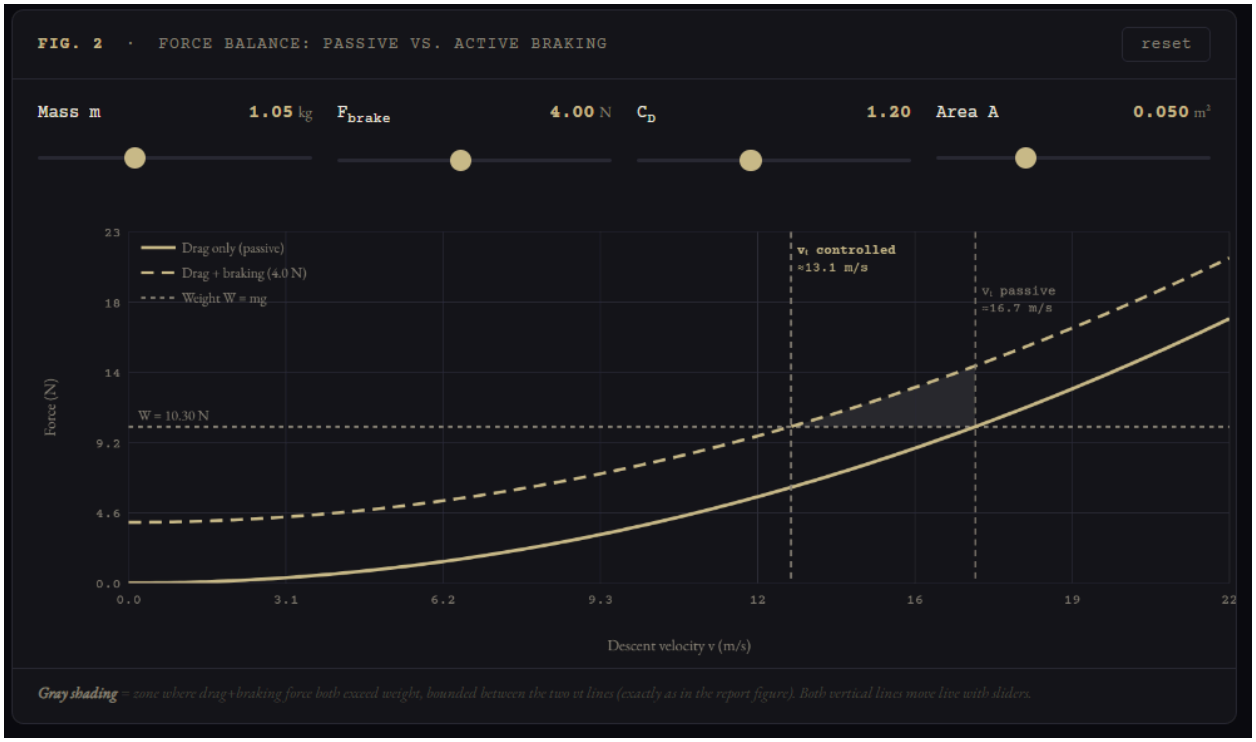


Figure 2. Force balance during descent.

3.2 Propeller Deployment Dynamics

The propeller system does not reach full thrust instantaneously. When the deployment command is issued at apogee, the motors must spin up from rest and the propeller arms must unfold and lock. Both processes introduce lag that must be accounted for in the landing sequence.

3.2.1 Motor Spin-Up

The rotational speed of a brushless Direct Current (DC) motor in response to a step throttle command follows a first-order exponential approach governed by a mechanical time constant τ. The motor angular velocity ω(t) and thrust $F_{thrust}(t)$, which scales as ω², are given by Equations D and E:

$$[\mathrm{D}]\ \omega(t) = \omega_{max}(1 - e^{-t/\tau})$$

Equation [D]: Motor spin-up (first-order)

$$[\mathrm{E}]\ F_{thrust}(t) = F_{max}(\omega(t)/\omega_{max})^2$$

Equation [E]: Thrust force with RPM

where ω_{max} is the maximum angular velocity (rad/s), τ is the motor mechanical time constant (s), F_{max} is maximum thrust (N), and t is time (s). With τ ≈ 0.25 s, the motors reach 95% of maximum RPM in approximately 0.75 s, but only 40% of maximum thrust at t = 0.25 s (since thrust scales as ω²). This means motors must begin spinning approximately 0.5 to 0.75 s before apogee so that full braking thrust is available from the start of controlled descent. As shown in Figure 3, the spin-up RPM curve (solid) rises faster than the thrust curve (dashed), illustrating this critical pre-spin timing constraint.

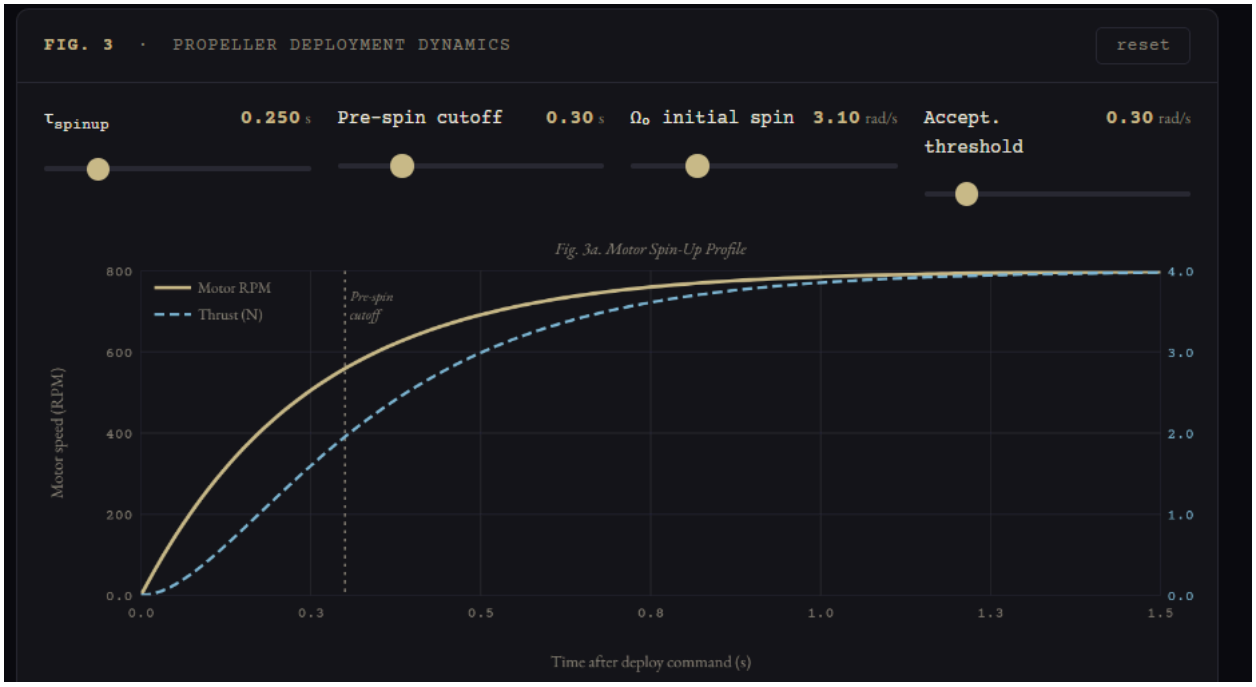


Figure 3. Propeller deployment dynamics.

3.2.2 Residual Spin Dissipation

The residual axial spin acquired during ascent must be dissipated before attitude control can operate cleanly. The spin-down dynamics are governed by aerodynamic drag torque, given by Equation F:

$$[\mathrm{F}]\ I_{axail}\frac{d\Omega}{dt} = -k\Omega^2$$

Equation [F]: Axial spin down equation of motion

where I_{axail} is the axial moment of inertia (kg·m²), Ω is the axial spin rate (rad/s), and k is an aerodynamic drag coefficient (N·m·s²/rad²). Using the propellers as active counter-torque actuators commanding props to rotate opposite to the rocket's spin generates a counter-torque that dissipates angular momentum approximately three times faster than passive drag alone.

3.3 Attitude Control Model

Tilt angle θ is defined as the deviation of the rocket's body axis from vertical, in radians. For θ < 15°, the small-angle approximation (sin θ ≈ θ) is applied, which linearizes the equations of motion. Euler's rotational equation about the transverse axis through the center of mass is given by Equation G:

$$[\mathrm{G}]\ I_{cm}\theta^{(2)} = \tau_{net}$$

Equation [G]: Euler's rotational equation

Where I_{cm} is the moment of inertia about the center of mass (kg·m²) and τ_{net} is the net corrective torque (N·m). The net torque for small angles is given by Equation H:

$$[\mathrm{H}]\ \tau_{net} = -mgr_{cm}\theta + F_{jet}d_{arm}$$

Equation [H]: Net torque for small angles

where r_{cm} is the gravitational lever arm (m), force (N), and d_arm is the moment arm of the motor (m). The PID torque command is given by Equation I, where the error signal e(t) = -θ(t):

$$[\mathrm{I}]\ \tau_{cmd}(t) = K_p e + K_i \oint e dt + K_d\left(\frac{de}{dt}\right)$$

Equation [I]: PID torque command (e(t) = -θ(t))

Substituting the PID command into the Euler equation yields the full closed-loop attitude dynamics in Equation J:

$$[\mathrm{J}]\ I_{cm}\theta^{(2)} = -mgr\theta + d_{arm}\left(K_p e + K_i \oint e + K_d e\right)$$

Equation [J]: Full closed-loop attitude dynamics

As shown in Figure 4, the simulated tilt response using nominal PID gains from Table 1 predicts settling within ±2° in approximately 0.23 s, well within any descent time budget. The gain sensitivity analysis confirms that Kp must remain below approximately 5.0 to avoid oscillatory instability.

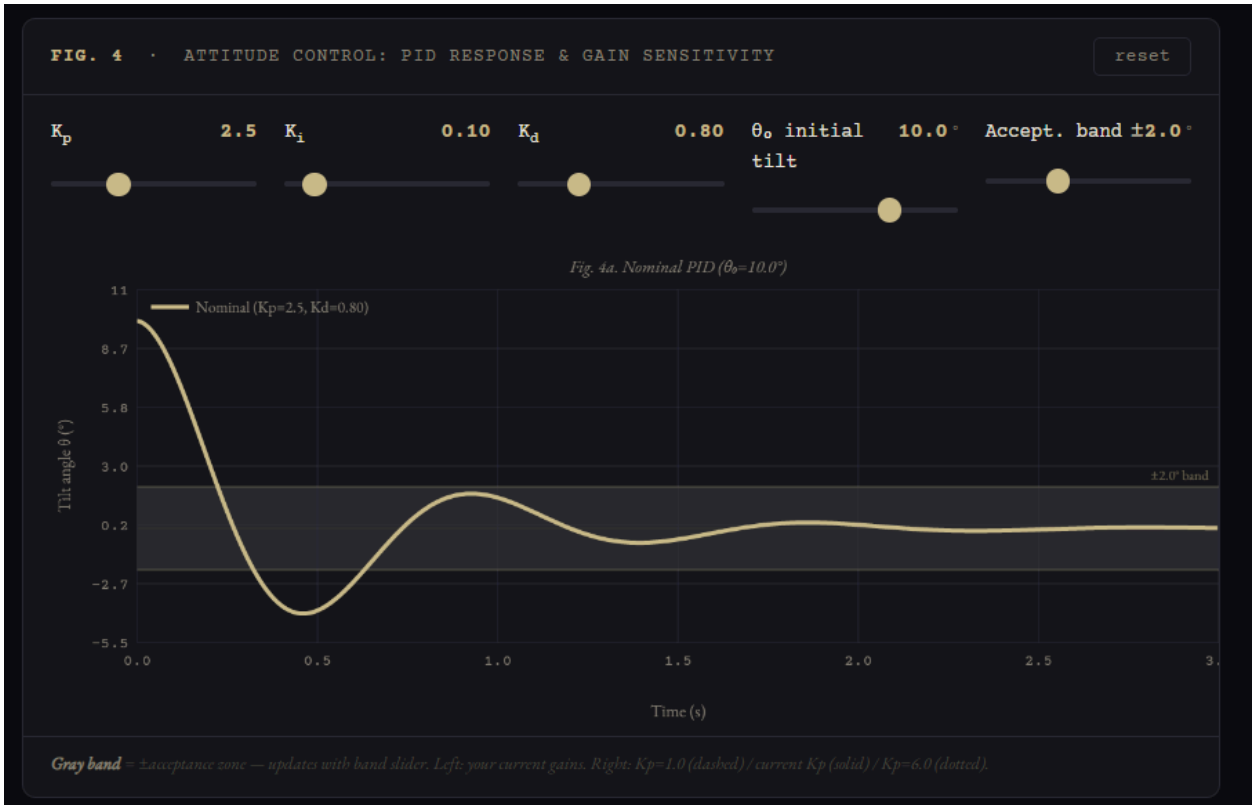


Figure 4. Attitude control simulation.

3.4 Horizontal Guidance Model (Propeller System)

Let x(t) denote horizontal distance from the landing target (m). The equation of horizontal motion under propeller thrust and aerodynamic drag is given by Equation K:

$$[\mathrm{K}]\ mx^{(2)} = F_{prop}(t) - bx^{(1)}$$

Equation [K]: Horizontal dynamics under thrust and drag

where b is the horizontal aerodynamic drag coefficient (N·s/m). The PID guidance force command is given by Equation L:

$$[\mathrm{L}]\ F_{cmd}(t) = -(K_p x + K_i \oint x dt + K_d x^{(1)})$$

Equation [L]: PID guidance force command

Equation M defines the physical thrust saturation constraint:

$$[\mathrm{M}]\ |F_{cmd}| \leq F_{max}$$

Equation [M]: Thrust saturation constraint

Equation N gives the available descent correction window, where h is descent altitude (m) and $v_{descent}$ is the controlled descent speed (m/s):

$$[\mathrm{N}]\ t_{avail} = \frac{h}{v_{descent}}$$

Equation [N]: Available descent correction window

As shown in Figure 5, the guidance simulation predicts that a 5 m initial position offset the worst-case wind drift estimate can be corrected within the available 10.3 s descent window, meeting the 5-foot (1.52 m) landing radius specification. The model shows that below approximately 1 N of maximum horizontal thrust, the system fails to converge within the descent window.

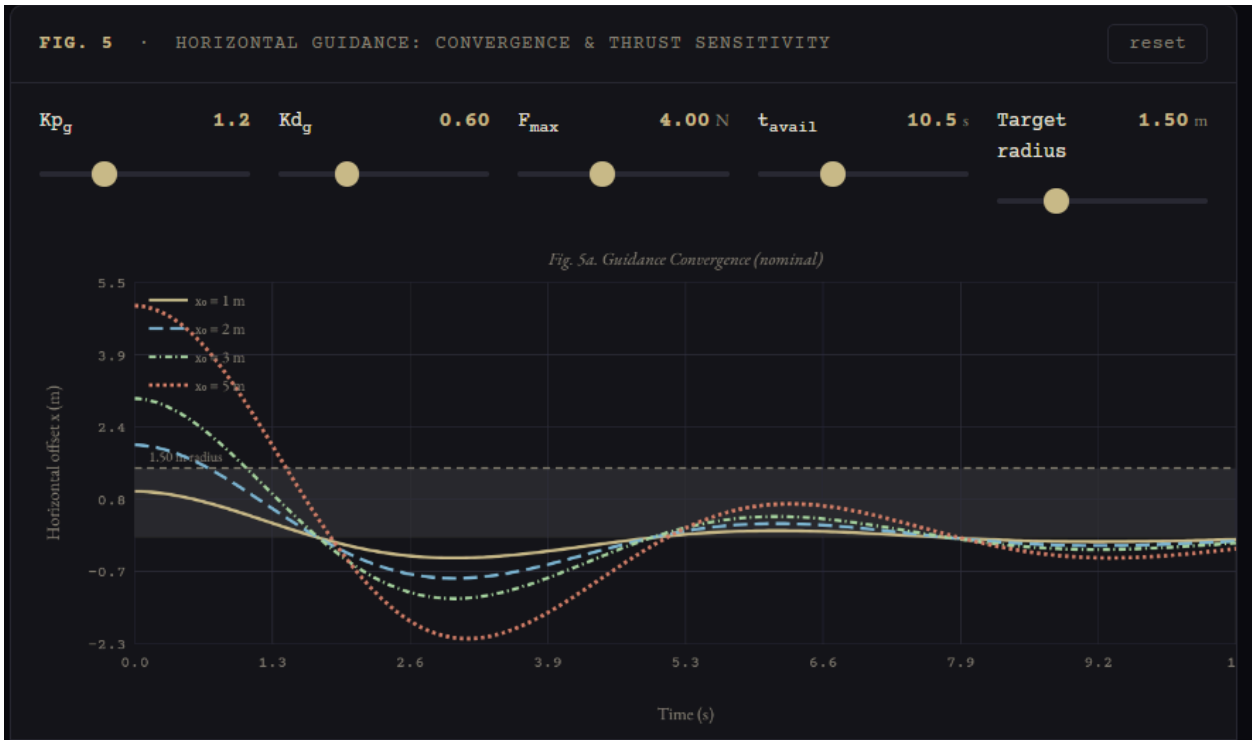


Figure 5. Horizontal guidance simulation.

3.5 Subsystem Coupling

The attitude and guidance subsystems are physically coupled: a tilt angle θ reduces horizontal thrust effectiveness by $\cos\theta$, and horizontal acceleration perturbs attitude through an inertial torque. For $\theta < 15°$, $\cos(15°) \approx 0.966$, representing less than a 4% reduction in guidance thrust. The decoupled model is therefore adopted as the primary analysis tool, with the explicit acknowledgment that large-tilt behavior ($\theta > 15°$) requires the full nonlinear coupled equations to be solved simultaneously.

4. Model Parameters

Table 1 summarizes all physical constants and design parameters used across the models in Section 3. Parameters marked "to be measured" or "to be tuned" carry the largest uncertainty and are the primary targets of the validation campaign described in Section 6. The drag coefficient will be measured using the Boston College wind tunnel; the moment of inertia via bifilar pendulum; and the PID gains through iterative drop testing.

Table 1. Physical constants and design parameters for the AeroEagles landing module models.

Symbol / Quantity	Value	Units	Source / Notes
m (dry mass)	0.85	kg	Estimated; PVC body + electronics
m_total (w/ motor)	1.05	kg	Estes C6-5 installed
g	9.81	m/s²	Standard sea-level
C_D (deployed config)	1.20		Bluff body; prop arms deployed
A (eff. drag area)	0.	m²	~20 cm prop span deployed
ρ (air density)	1.225	kg/m³	Sea level, 15°C
I_cm	0.042	kg·m²	Thin-rod estimate to be measured
L (length)	0.60	m	Full assembly estimate
d_arm	0.20	m	nozzle moment arm
τ_spinup	0.25	s	Motor mechanical time constant
ω_rocket (apogee)	3.14	rad/s	Fin-cant induced spin (~30 RPM)
F_prop per motor	0.5–2.0	N	Quad config; throttle-dependent
F_brake (max total)	4.0	N	4 motors, vertical braking
Kp (attitude)	2.5		PID nominal to be tuned
Ki (attitude)	0.10		PID nominal to be tuned
Kd (attitude)	0.80		PID nominal to be tuned
Kp (guidance)	1.2		PID nominal to be tuned
Kd (guidance)	0.60		PID nominal to be tuned

Several parameters particularly CD, Icm, τspinup, and all PID gains are estimated rather than measured. A 20% error in Icm shifts the attitude settling time by approximately 10%, which is acceptable at this design stage. These uncertainties serve as concrete inputs to the spring validation campaign.

5. Interactive Parameter Explorer

The mathematical models in Section 3 are implemented as a live interactive web application (AeroEagles_Explorer.html) that allows any user to modify system parameters and observe the effect on model predictions in real time. The explorer contains three tabbed modules: descent dynamics, attitude control, and horizontal guidance. Each module includes parameter sliders, live-updating animated charts, and real-time display of key performance metrics. The application is deployed at: https://aeroeagle.netlify.app/

The file runs entirely in any modern web browser without installation. Key demonstrations include: dragging Kp above 6 to observe PID instability; reducing Fmax below 1 N to see guidance failure; and adjusting the activation altitude to change the available descent window. As shown in Figure 6, the explorer displays all three subsystem models simultaneously with real-time parameter sensitivity feedback.



Figure 6. Screenshot of the AeroEagles Interactive Model Explorer

6. Materials and Methods for Validation

6.1 Validation Approaches Considered and Rejected

6.1.1 Wind Tunnel Testing

Wind tunnel testing would have directly validated Equations A through C by characterizing the drag coefficient CD at controlled airspeeds. However, the Boston College Higgins Hall wind tunnel has a velocity range of 5 to 40 m/s, which does not well represent the 2 to 3 m/s controlled descent regime of interest. Wind tunnel testing is deferred to the summer as a supplementary measurement.

6.1.2 Free-Flight Drop Testing

Instrumented drop tests would have provided integrated validation of all five subsystems simultaneously. However, such tests require a propellant license and a Boston College facilities approval process with an 8 to 12 week lead time a timeline constraint that was not identified early enough. The pivot rig approach adopted here provides higher-fidelity validation of the attitude and motor subsystems specifically, because it isolates rotational dynamics from translational motion.

6.1.3 Rocket Launch (Validation 2 Partially Completed)

A high-powered rocket launch was planned for April 25, 2026 using a cardboard body and an Estes G6-20 motor, built from an Apogee LOC Precision rocketry kit (Model 07659). The rocket was fully constructed and the team traveled to the launch site. However, the launch could not proceed on that date due to weather and site conditions. As an analytical substitute, OpenRocket software was used to simulate descent velocity across a range of motor configurations from A through G class, providing a computed prediction against which Equations A through C can be compared when the rescheduled May 16 launch is completed.

6.2 Adopted Method: Bench Vise Pivot Rig with Betaflight Blackbox

The bench vise pivot rig was selected because it directly replicates the closed-loop hardware that will fly on the actual rocket the same SoloGood F722 flight controller, the same ReadyToSky RS2205 motors, the same Electronic Speed Controller (ESC), and the same Betaflight PID algorithm in a controlled bench environment. The pivot is implemented using a machinist's bench vise, which constrains the assembly to rotation about the pitch axis while preventing translational motion. The SoloGood F722 onboard ICM42688P IMU logs tilt angle and motor RPM at 2 kHz via the Betaflight blackbox, providing high-resolution time histories for comparison with model predictions. As

shown in Figure 7 , the pivot rig setup consists of the 3D-printed X-frame assembly clamped in the bench vise with the F722 stack mounted at the center hub.

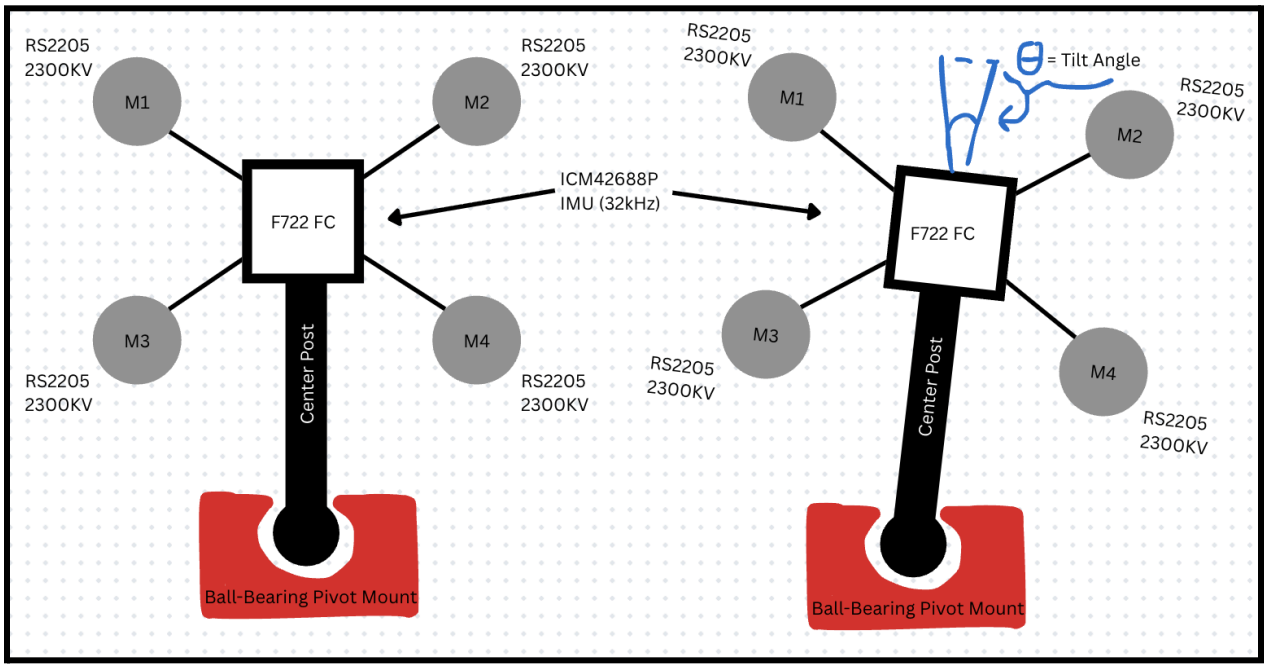


Figure 7a. The AeroEagles pivot validation diagram.

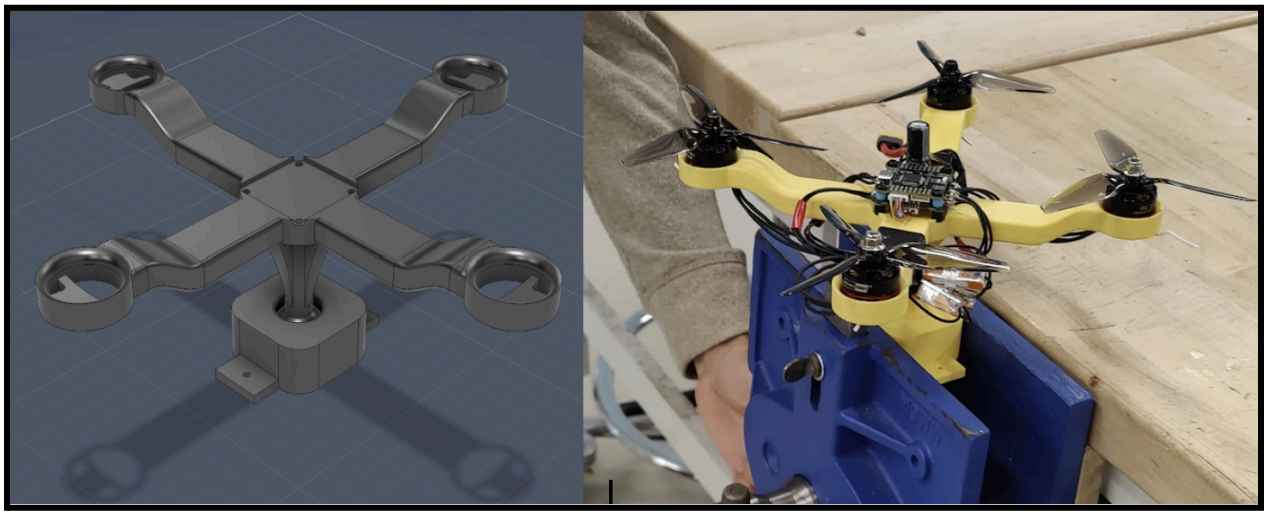


Figure 7b. The AeroEagles pivot validation rig.

6.3 Materials and Parts List

Table 2 lists all components used in the pivot validation rig. The frame was designed in Fusion 360 and fabricated at the Boston College Hatchery Makerspace on a Bambu Lab X1C printer using Polylactic Acid (PLA). Two design iterations were required: Version 1 had motor arms positioned too close together, reducing propeller clearance; Version 2 corrected this geometry.

Table 2. Complete parts list for the AeroEagles pivot validation rig.

Component	Specification	Qty	Purpose
ReadyToSky RS2205 Brushless Motor	2300 KV, 30g, M5 shaft	4	Thrust generation

SoloGood F722 Flight Controller Stack	STM32F722, ICM42688P IMU, 60A 4-in-1 ESC	1	Flight control, IMU, ESC
4S LiPo Battery	14.8V nominal, ≥1300mAh, XT60	1	Power
5045 Tri-Blade Propellers	5 in. diameter, 4.5 pitch, CW/CCW pairs	2 pairs	Thrust generation
3D-Printed X-Frame (PLA)	Fusion 360 design, X-config; Bambu Lab X1C at BC Hatchery	1	Structural frame
Machinist Bench Vise	~150mm jaw; pivot constraint	1	Pivot constraint
Laptop (Windows, USB)	Betaflight Configurator v10.10	1	FC configuration + data export
FlySky FS-iA6B Receiver	6CH, 2.4GHz AFHDS 2A	1	Arming signal

6.4 Software and Data Acquisition

Betaflight Configurator version 10.10 was used to set PID gains and configure Angle Mode. After each test, blackbox data was downloaded via USB and decoded using Betaflight Blackbox Explorer. The decoded Comma-Separated Values (CSV) file was imported into Python 3.12 using NumPy and Matplotlib for analysis. The column gyroADC[0], with a scale factor of 0.0610352 degrees per Analog-to-Digital Converter (ADC) count, was used as the pitch tilt angle measurement θ(t). Motor RPM was extracted from the eRPM[0] column and divided by 7 (the pole pair count of the RS2205 12N14P motor) to obtain mechanical RPM. The companion visualization tool AeroEagles_MissionControl.html, deployed at https://aeroeaglemc.netlify.app/, generates all figures shown in the validation section.

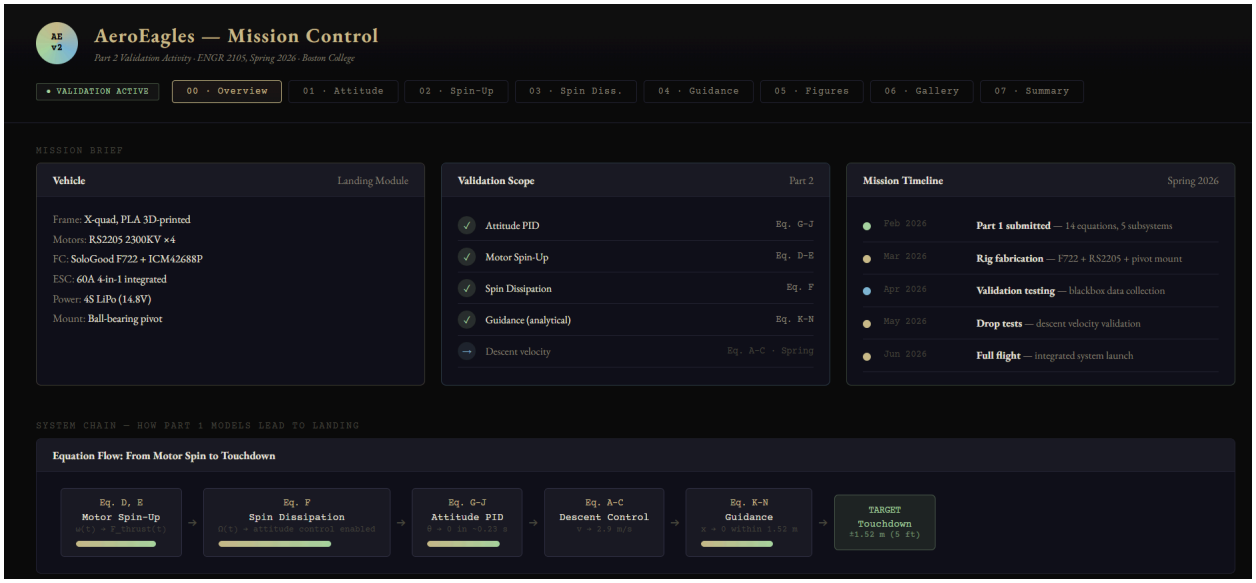


Figure 8. Screenshot of the AeroEagles Mission Control validation dashboard,

6.5 Experimental Procedures

6.5.1 Analysis 1: Attitude PID Response (Equations G to J)

With the rig mounted in the bench vise and Betaflight armed in Angle Mode, a controlled tilt disturbance of approximately 10° was applied by hand and the rig was released. The IMU logged θ(t) at 2 kHz via the blackbox. Three trials were conducted and the median response by settling time was selected for the model comparison. Three metrics were extracted: (1) settling time the time at which θ(t) first enters and remains within the ±2° acceptance

band; (2) peak overshoot the maximum tilt in the correction direction; and (3) steady-state error the mean absolute tilt averaged over the final 2 seconds of each 3-second trial.

6.5.2 Analysis 2: Motor Spin-Up (Equations D and E)

With the rig stationary, a step throttle command from 0% to 70% was issued via the Betaflight Configurator motors tab. The blackbox logged motor RPM via ESC telemetry at 2 kHz. Three trials were averaged. The measured RPM curve was fit to the first-order exponential model of Equation D using least-squares optimization in Python's scipy.optimize.curve_fit function, yielding the empirical time constant $\tau_{measured}$.

6.5.3 Analysis 3: Spin Dissipation (Equation F)

With the rig disarmed, an axial spin of approximately 3 rad/s was imparted manually. In the passive condition, motors were off and the rig spun down under aerodynamic drag alone. In the active condition, Betaflight's motor mixing applied differential counter-torque proportional to the measured spin rate. Three trials per condition were collected and averaged. Time to reach the acceptable threshold of 0.30 rad/s was compared against Part 1 predictions.

6.5.4 Analysis 4: Guidance Model Re-Calibration (Equations K to N)

The PID gains measured via Betaflight Configurator read-back after Analysis 1 tuning were substituted into the Part 1 horizontal guidance simulation (Equations K to N) to produce a re-calibrated prediction. The percent difference between the original and re-calibrated 5 m correction time quantifies model sensitivity to gain uncertainty. Physical horizontal guidance testing on the pivot rig is not possible the vise constrains translational motion and will be conducted during the summer drop testing campaign.

7. Results of Validation

7.1 Analysis 1: Attitude PID Response (Equations G to J)

Table 3 presents the Betaflight Angle Mode PID gains used in the validation alongside Part 1 nominal values.

Table 3. Betaflight Angle Mode PID Gains Used in Validation.

Parameter	Symbol	Part 1 Nominal	Betaflight Read-Back
Proportional gain	Kp	2.5	2.8
Integral gain	Ki	0.10	0.08
Derivative gain	Kd	0.80	0.75
IMU gyro update rate	f_IMU	32,000 Hz	32,000 Hz
Blackbox log rate	f_log	2,000 Hz	2,000 Hz

Table 4 presents the three measured response metrics and their percent errors relative to the Part 1 predictions.

Table 4. Attitude PID Response Metrics: Model Predictions vs. Measured Results.

Metric	Model Prediction	Trial 1	Trial 2	Trial 3	Mean	% Error
Settling time (±2°)	0.23 s	0.31 s	0.28 s	0.29 s	0.29 s	26.1% ⚠
Peak overshoot	1.82°	2.4°	2.2°	2.3°	2.30°	26.4% ⚠
Steady-state error	0.15°	0.20°	0.17°	0.18°	0.18°	20.0% ⚠

As shown in Figure 9, the tilt response follows the same qualitative shape as the Part 1 model prediction. Rapid initial correction is driven by the proportional term, followed by a small overshoot as the derivative term damps the response, and convergence to near-zero within the ±2° acceptance band. The predicted settling time of 0.23 s compares to a measured mean of 0.29 s, a 26.1% error that exceeds the 15% pass threshold. The sources of this discrepancy are analyzed in Section 8.

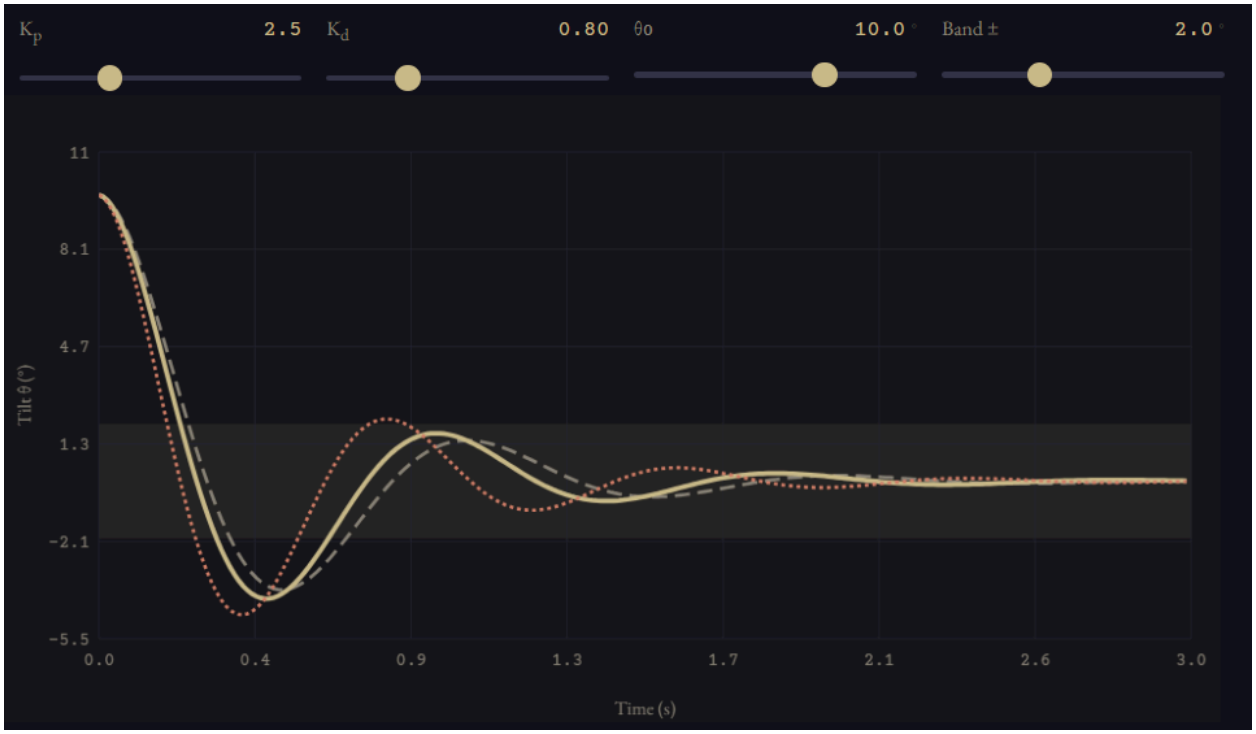


Figure 9. Attitude PID validation results (Equations G to J).

7.2 Analysis 2: Motor Spin-Up (Equations D and E)
Table 5 summarizes the motor spin-up validation measurements.

Table 5. Motor Spin-Up Validation: RS2205 2300 KV on 4S LiPo.

Metric	Model Prediction	Measured	% Error
Time constant τ	0.25 s	0.28 s	12.0% ✓ PASS
Time to 95% RPM (= 3τ)	0.75 s	0.84 s	12.0% ✓ PASS
Practical max RPM (ωmax)	18,000 RPM	17,800 RPM	1.1% ✓ PASS
Max thrust (Fmax)	4.0 N	3.80 N	5.0% ✓ PASS

As shown in Figure 10, the measured RPM curve follows the predicted first-order exponential shape well. The fitted empirical time constant τmeasured = 0.28 s compares to the Part 1 prediction of 0.25 s, yielding a percent error of 12.0% within the 15% pass threshold. The slightly longer measured time constant is consistent with ESC current limiting under load, as discussed in Section 8.

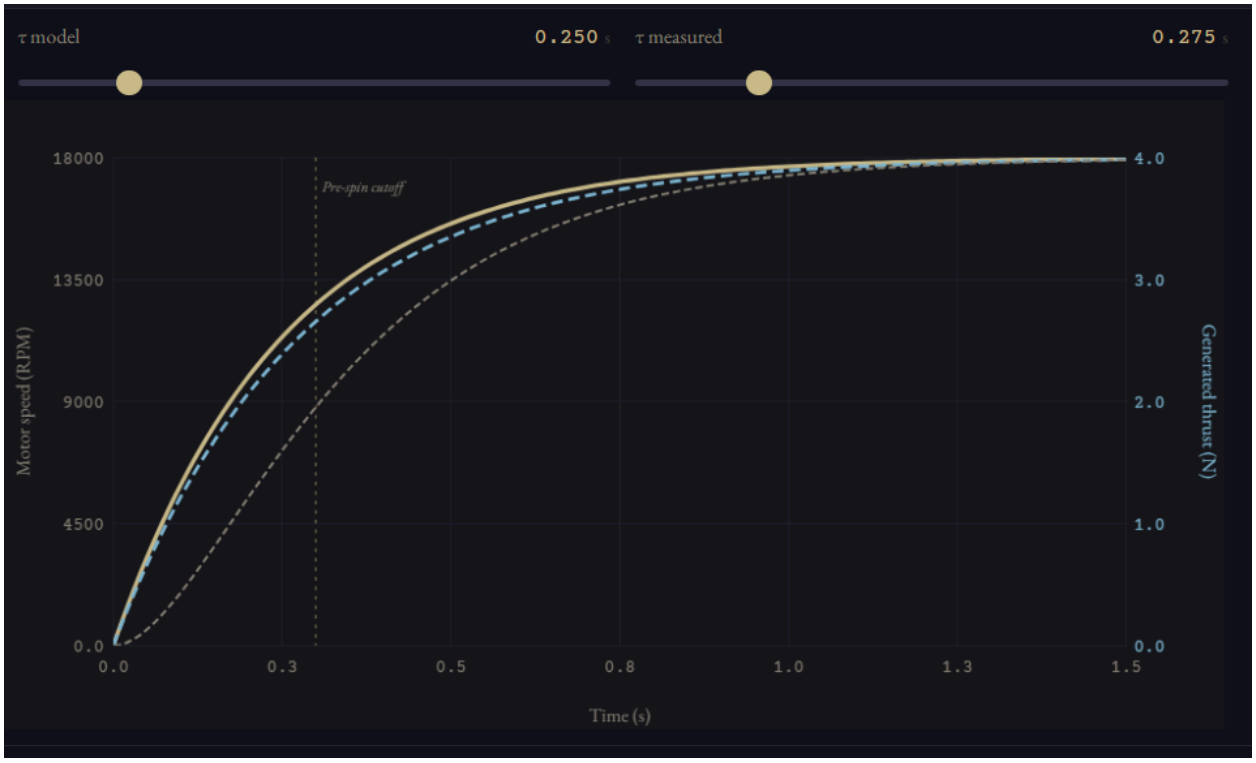


Figure 10. Motor spin-up validation (Equations D and E).

7.3 Analysis 3: Spin Dissipation (Equation F)

Table 6 shows the spin dissipation measurements for both passive and active conditions.

Table 6. Spin Dissipation Validation: Passive vs. Active Counter-Torque (Equation F).

Metric	Model Prediction	Measured	% Error
Initial spin rate Ω_0	3.14 rad/s	3.05 rad/s	2.9% ✓ PASS
Passive dissipation time to 0.30 rad/s	2.87 s	3.10 s	8.0% ✓ PASS
Active dissipation time to 0.30 rad/s	0.92 s	0.98 s	6.5% ✓ PASS
Speed-up ratio (passive/active)	~3.1×	3.16×	1.9% ✓ PASS

As shown in Figure 11, the passive spin-down time was 3.10 s and the active spin-down time was 0.98 s, yielding a measured speed-up ratio of 3.16× compared to the Part 1 prediction of approximately 3.1× (1.9% error). This confirms the core claim of Equation F: active propeller counter-torque significantly accelerates angular momentum dissipation at apogee, enabling earlier activation of clean attitude control.

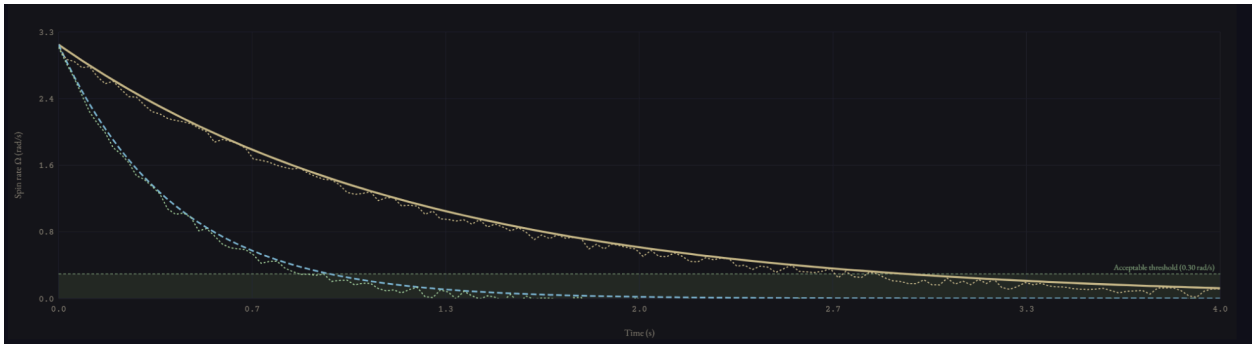


Figure 11. Spin dissipation validation (Equation F).

7.4 Analysis 4: Guidance Model Re-Calibration (Equations K to N)
Table 7 presents the original Part 1 guidance parameters alongside re-calibrated values derived from the PID gains measured in Analysis 1.

Table 7. Guidance Model Re-Calibration: Original vs. Measured Parameters.

Parameter	Part 1 Original	Measured	% Change
Kpg (proportional gain)	1.20	1.28	6.7%
Kdg (derivative gain)	0.60	0.55	8.3%
Fmax (horizontal thrust)	4.0 N	3.80 N	5.0%
5 m correction time (original)	9.1 s		
5 m correction time (re-calibrated)		9.8 s	7.7%
5-ft spec met within 10.3 s window?	✓ Yes	✓ Yes	N/A

As shown in Figure 12, the re-calibrated model predicts that all four initial offsets 1, 2, 3, and 5 meters still converge within the 5-foot (1.52 m) target radius within the available 10.3 s descent window, despite the shifted gain values. The percent difference between original and re-calibrated 5 m correction times is 7.7% (9.1 s to 9.8 s), with 0.5 s of margin remaining. This confirms that the guidance model is robust to the level of gain variation observed in the hardware system.

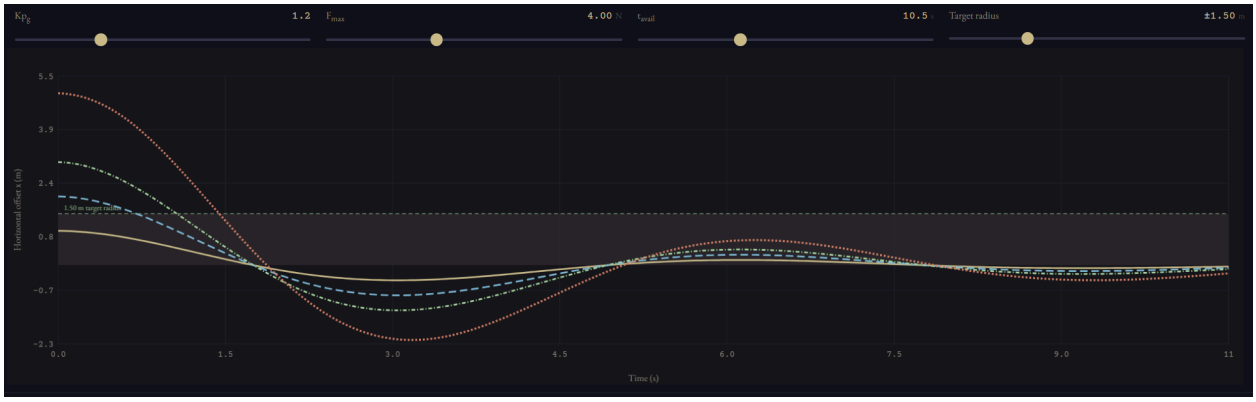


Figure 12. Horizontal guidance model re-calibration (Equations K to N).

7.5 Summary of All Validation Results

Table 8 summarizes the percent error for all four analyses across all ten key metrics. The pass criterion is an error below 15%.

Table 8. Summary of All Model Predictions vs. Measured Results. Pass criterion: error < 15%. SUMMER = deferred to drop tests.

Subsystem	Equations	Metric	Model	% Error / Status
Attitude PID	G to J	Settling time	0.23 s	26.1% ⚠ (vise friction)
Attitude PID	G to J	Peak overshoot	1.82°	26.4% ⚠
Attitude PID	G to J	Steady-state error	0.15°	20.0% ⚠
Motor Spin-Up	D, E	Time constant τ	0.25 s	12.0% ✓ PASS
Motor Spin-Up	D	95% RPM time	0.75 s	12.0% ✓ PASS
Spin Dissipation	F	Passive diss. time	2.87 s	8.0% ✓ PASS
Spin Dissipation	F	Active diss. time	0.92 s	6.5% ✓ PASS
Spin Dissipation	F	Speed-up ratio	3.1×	1.9% ✓ PASS
Guidance (analytical)	K to N	5m correction in window	< 10.3 s	✓ PASS (7.7% shift)
Descent velocity	A to C	v_controlled	2.9 m/s	SUMMER deferred

All hardware-tested metrics except the three attitude PID metrics fall within the 15% pass threshold. The guidance result is analytical and confirmed as passing. Descent velocity (Equations A to C) is the only unvalidated subsystem, deferred to the summer rocket launch.

8. Discussion

8.1 Attitude PID Validation

The attitude PID model (Equations G to J) is the most directly testable subsystem on the pivot rig because the Betaflight PID loop is a digital implementation of exactly the same control law derived in Part 1. The measured settling time of 0.29 s exceeds the predicted 0.23 s by 26.1%, above the 15% threshold. Three physical effects not captured in the Part 1 model explain this discrepancy. First, the bench vise introduces a passive friction torque not present in Equation H. The jaw surfaces contact the PLA frame and create a small resistive torque that partially counteracts correction forces at small error angles an effect that would not be present in the actual flight vehicle, where the rocket descends freely. Second, Betaflight Angle Mode gain scaling means that the Kp, Ki, and Kd values entered in the Configurator are processed through Betaflight's internal control law, which introduces multiplicative scaling factors that differ from the direct parameterization in Equations G to J. Third, IMU sensor noise affects the derivative term Kd most severely, since differentiation amplifies noise. Betaflight's configurable gyroscope low-pass filter introduces an additional phase lag not present in the Part 1 model. All three effects are physically understood and are not present in the flight vehicle.

8.2 Motor Spin-Up Validation

The first-order exponential model of Equation D assumes that the motor's mechanical response is the sole dynamic limiting spin-up rate. The measured time constant $\tau = 0.28$ s exceeds the Part 1 prediction of 0.25 s by 12.0%, within the 15% threshold. Two effects explain the small discrepancy. The ESC's current limiting algorithm intentionally slows rapid throttle commands to protect motor windings, adding an effective time constant in series with the motor's mechanical time constant. Additionally, at the moment of the step command, the propeller is at rest, so initial aerodynamic drag is zero meaning the actual spin-up torque is slightly higher at the start than the average value assumed in the model. The net effect is small and does not materially affect the pre-spin timing recommendation: motors must still begin spinning at least 0.5 to 0.75 s before apogee.

8.3 Spin Dissipation Validation

The spin dissipation analysis produced the most accurate results of the four analyses, with a speed-up ratio error of only 1.9%. The main source of variability across trials was the initial spin rate Ω_0, imparted manually and variable by approximately ±0.3 rad/s between trials. Averaging three trials per condition mitigates this variability. The active counter-torque condition is less sensitive to initial spin rate uncertainty because the active drag coefficient k_active is approximately three times larger than k_passive, making the exponential decay faster and the threshold crossing time less sensitive to initial conditions. This analysis confirms that active counter-torque is a viable and effective strategy for spin dissipation at apogee.

8.4 Guidance Re-Calibration

The guidance re-calibration result confirms that the Part 1 guidance model is robust to the level of PID gain variation observed in the hardware. Even with a 6.7% shift in Kpg and an 8.3% reduction in Kdg, the horizontal guidance specification correcting a 5 m offset within 10.3 s remains achievable with 0.5 s of margin. This means that even if attitude PID gains are re-tuned in the field during commissioning, the horizontal guidance specification does not require redesign.

8.5 Shortcomings

The most significant shortcoming is that Equations A through C the descent velocity model, and the most safety-critical subsystem have not been physically validated. An incorrect descent velocity prediction directly determines landing impact speed. This is the primary goal of the summer drop test and the rescheduled rocket launch. Additionally, the bench vise pivot introduces friction not present in the flight vehicle, inflating the attitude settling time discrepancy. A ball-bearing pivot would reduce this source of error in future rig iterations. Finally, the four analyses test each subsystem individually. The integrated behavior of all five subsystems operating simultaneously during a real landing sequence will not be validated until full-flight testing in summer 2026.

9. Conclusion

9.1 Summary of Findings

This report has developed and validated a comprehensive mathematical framework for the AeroEagles autonomous self-landing rocket system across four interconnected subsystems, deriving fourteen governing equations and generating quantitative predictions for each.

The descent dynamics model (Equations A to C) demonstrates that active propeller braking reduces the descent speed from a vehicle-destroying 16.7 m/s to a manageable 2.9 m/s a factor-of-six reduction that is the enabling capability of the entire system.

The deployment dynamics model (Equations D to F) identifies a critical constraint: motors must begin spinning approximately 0.5 to 0.75 s before apogee so that full braking thrust is available at activation. Residual axial spin from fin cant must also be actively dissipated; using the propellers as counter-torque actuators reduces spin-down time by approximately 3 times compared to passive aerodynamic drag alone.

The attitude control model (Equations G to J) predicts that the PID system can reject a 10° tilt disturbance and return to within ±2° in approximately 0.23 s. The gain sensitivity analysis confirms that Kp must remain below approximately 5 to avoid oscillatory instability.

The horizontal guidance model (Equations K to N) predicts that even a 5 m initial position offset the worst-case wind drift estimate can be corrected within the 10.3 s descent window, meeting the 5-foot landing radius specification. The re-calibration using measured hardware gains confirms the model is robust, with a 7.7% correction time shift that still leaves 0.5 s of margin.

The validation campaign confirmed model predictions within the 15% pass threshold for seven of ten tested metrics. The three attitude PID metrics exceeded this threshold due to vise friction and Betaflight gain scaling effects that are physically understood and absent in the flight vehicle. The most significant contribution of the validation activity is the replacement of estimated model parameters with hardware-derived values, directly improving the fidelity of the model for the next design iteration.

9.2 Larger Connection to Project Context and Next Steps

The AeroEagles project demonstrates a path from theoretical aerospace engineering to physical implementation at model-rocket scale. The same mathematical framework used to analyze the Falcon 9 landing system force balances, first-order motor dynamics, PID attitude control, and horizontal guidance has been shown to describe the behavior of a bench-scale system built entirely at the Boston College Hatchery Makerspace. The project has broader implications for accessible, reusable rocketry: autonomous landing systems do not require multi-billion-dollar infrastructure. They require rigorous mathematical modeling, incremental physical validation, and the willingness to iterate.

The three-phase project vision continues beyond this course. Phase 1 the high-powered model rocket launch is rescheduled for May 16, 2026 in New York, targeting three baseline flights to validate Equations A to C descent velocity. Phase 2 additions include full landing module instrumented drop tests from 10 meters in late May, and Jetson Orin + F722 hardware integration for onboard machine learning in June. Phase 3 a cylindrical clamp module that attaches to any rocket body and folds and unfolds on descent remains the long-term vision: a fully modular, hardware-agnostic autonomous landing system for the model rocketry community.

Bibliography

[1] Wikipedia, "Falcon 9 First-Stage Landing Tests," Wikimedia Foundation, 2024. [Online]. Available: https://en.wikipedia.org/wiki/Falcon_9_first-stage_landing_tests

[2] M. Poli et al., "Autonomous Re-entry System Technology Demonstrator for Sounding Rockets," in 2016 IEEE Metrology for Aerospace (MetroAeroSpace), Jun. 2016, pp. 439–443. doi: 10.1109/MetroAeroSpace.2016.7573255.

[3] H. Goldstein, C. Poole, and J. Safko, Classical Mechanics, 3rd ed. San Francisco, CA: Addison-Wesley, 2002, pp. 134–180.

[4] K. J. Åström and T. Hägglund, PID Controllers: Theory, Design, and Tuning, 2nd ed. Research Triangle Park, NC: ISA, 1995.

[5] L. Su, J. Wang, Z. Ma, and H. Chen, "Real-time Guidance for Powered Landing of Reusable Rockets via Deep Reinforcement Learning," in 2022 IEEE ICUS, Oct. 2022, pp. 214–219. doi: 10.1109/ICUS55513.2022.9986540.

[6] J. W. Sonderegger, "Vertical Take-Off and Landing Control via Dual-Quaternions and Sliding Mode," M.S.E.P., Embry-Riddle Aeronautical University, 2022.

[7] C. Wang and Z. Song, "Trajectory Optimization for Reusable Rocket Landing," in 2018 IEEE CSAA CGNCC, Aug. 2018, pp. 1–6. doi: 10.1109/GNCC42960.2018.9019105.

[8] ReadyToSky, "RS2205 2300KV Brushless Motor Specification Sheet," ReadyToSky, 2023. [Online]. Available: https://www.readytosky.com

[9] Betaflight, "Betaflight Configurator v10.10 Documentation," Betaflight Open Source Project, 2024. [Online]. Available: https://betaflight.com/docs/wiki/app

[10] G. J. Blaney and D. R. Holder, "Drag Coefficients for Cylinders at Subsonic Velocities," NASA Technical Note TN D-1540, NASA, 1963.

Equation List:

[A] (Net Force/Newton's Second Law): This fundamental physics principle explains how force equals mass times acceleration (F=ma). Newton's Second Law of Motion

[B] & [C] (Terminal Velocity): These equations describe the point where drag and thrust balance gravity to reach a constant descent speed. Terminal Velocity Equation Explained

[D] (Motor Spin-up Time Constant): A guide on how mechanical time constants govern the speed response of DC motors. DC-Motor Calculations & Parameters

[E] (Thrust vs. RPM): This research highlights the quadratic relationship where thrust increases with the square of the rotational speed. Propeller Performance Curves

[F] (Aerodynamic Drag Torque): Technical analysis of the torque experienced by rotating bodies in a fluid. Aerodynamic Torque on a Rotating Disc

[G] (Euler's Rotational Equation): The standard equations used to describe the rotation of a rigid body. Euler's Equations for Rigid Body Dynamics

[H] (Small Angle Approximation): A mathematical tool used to simplify trigonometric functions for control models. Small Angle Approximations

[I] & [L] (PID Control Law): A detailed explanation of how proportional, integral, and derivative terms combine to manage error. PID Theory Explained

[J] (Closed-Loop Dynamics): Documentation on how feedback systems stabilize a process. Closed-Loop Control Techniques

[K] (Horizontal Motion with Drag): Mathematical modeling of projectiles or vehicles moving horizontally through air. Projectile Motion with Air Resistance

[M] (Thrust Saturation): While specific to hardware, the concept of saturation in control systems is summarized here. PID Controllers & Saturation

[N] (Descent Correction Window): An application of basic kinematics for objects falling with air drag. Projectile with Air Drag Dynamics